Numerical simulations of a buoyant autocatalytic reaction front in tilted Hele-Shaw cells

N. Jarrige, I. Bou Malham, J. Martin, N. Rakotomalala, D. Salin, and L. Talon*

Lab FAST, Universite Pierre et Marie Curie-Paris 6–Universite Paris-Sud–CNRS, Bat. 502, rue du Belvedere, Campus Universitaire, Orsay F-91405, France

(Received 21 January 2010; published 22 June 2010)

We present a numerical analysis of solutal buoyancy effects on the shape and the velocity of autocatalytic reaction fronts, propagating in thin tilted rectangular channels. We use two-dimensional (2D) lattice Bathnagar-Gross-Krook (BGK) numerical simulations of gap-averaged equations for the flow and the concentration, namely a Stokes-Darcy equation coupled with an advection-diffusion-reaction equation. We do observe stationary-shaped fronts, spanning the width of the cell and propagating along the cell axis. We show that the model accounts rather well for experiments we performed using an Iodate Arsenous Acid reaction propagating in tilted Hele-Shaw cells, hence validating our 2D modelization of a three-dimensional problem. This modelization is also able to account for results found for another chemical reaction (chlorite tetrathionate) in a horizontal cell. In particular, we show that the shape and the traveling velocity of such fronts are linked with an eikonal equation. Moreover, we show that the front velocity varies nonmonotonically with the tilt of the cell, and nonlinearly with the width of the cell.

DOI: 10.1103/PhysRevE.81.066311 PACS number(s): 47.55.P−, 47.15.gp, 47.70.Fw, 82.40.Ck

I. INTRODUCTION

Autocatalytic reaction fronts between a reactant and a product may propagate as solitary waves, namely, at a constant velocity and with a stationary concentration profile, resulting from a balance between molecular diffusion and chemical reaction [1–5]. In most systems, the fluid left behind the front has a different density, leading potentially to buoyancy driven flows and instabilities [6–8]. The density contrast is also responsible for the variation of the velocity of an autocatalytic reaction front with the inclination of the tube [9]. This buoyancy driven effect was recently revisited with 2D numerical simulations of the Stokes regime [10] and with experiments in Hele-Shaw cells [11]. However, the scaling law of the front extension with the cell geometry obtained in [11] does not agree with the result of the Stokes simulations of [10]. The present work aims to investigate the scaling laws of the reaction front extension and velocity, for various cell inclinations. In order to do this, we use a 2D model for the propagation of an autocatalytic reaction front in rectangular channels (Hele-Shaw cells) in the presence of a density contrast. This model is simulated using a 2D lattice BGK method [12] and is validated by a comparison with experiments using the iodate arsenious acid (IAA). We then carry out a parametric study of the front velocity and extension, and we derive their scaling laws.

II. SYSTEM DESCRIPTION

For the sake of comparison, we chose an autocatalytic reaction currently used in experiments, namely, the IAA,

$$3H_3AsO_3 + IO_3^- + 5I^- \rightarrow 3H_3AsO_4 + 6I^-. \tag{1}$$

For this reaction, the concentration, c, of the autocatalytic product (iodide $[I^-]$) normalized by the initial concentration of iodate ($[IO_3^-]_0$), obeys the diffusion-reaction equation,

$$\frac{\partial c}{\partial t} = D_m \Delta c + \alpha c^2 (1 - c), \tag{2}$$

where D_m is the molecular diffusion coefficient and α is the kinetic rate coefficient of the reaction. In the absence of flow, a propagating one-dimensional (1D) stationary concentration profile, resulting from the balance between diffusion and chemical reaction, is obtained,

$$c(z,t) = \frac{1}{1 + \exp[(z - V_\chi t)/l_\chi]}, \tag{3}$$

$$V_\chi = \sqrt{\frac{\alpha D_m}{2}}, \tag{4}$$

$$l_\chi = \sqrt{\frac{2D_m}{\alpha}}, \tag{5}$$

where the coordinate z is along the direction of propagation, and V_χ and l_χ are the propagation velocity of the chemical reaction front and the front width, respectively.

However, the IAA reaction induces a solutal density change: the products are lighter than the reactants [13]. Therefore, a descending front is stabilized by buoyancy and propagates at the velocity V_χ, as a planar wave [given by Eq. (3)], whereas an ascending front may undergo a Rayleigh-Taylor instability [5,7,13]. Indeed the density contrast leads to an induced fluid flow of velocity $\vec{u}$, which changes Eq. (2) into an advection-diffusion-reaction (ADR) equation,

$$\frac{\partial c}{\partial t} + \vec{u} \cdot \vec{\nabla} c = D_m \Delta c + \alpha c^2 (1 - c). \tag{6}$$

The so-induced flow obeys the Navier-Stokes equation for a fluid of viscosity η (there is no change in viscosity in the chemical reaction) and of density $\rho(c)$,

*talon@fast.u-psud.fr

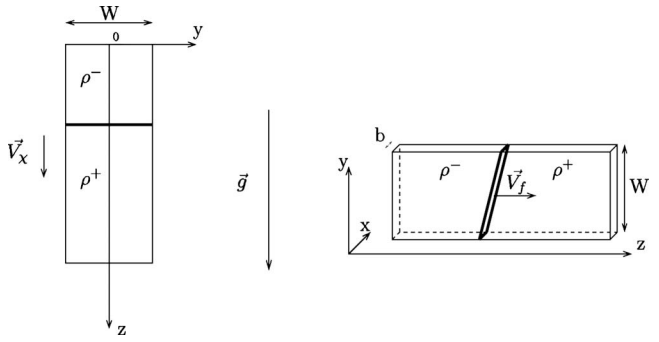

FIG. 1. Sketch of the autocatalytic reaction front observed in the plane (Oyz) of a Hele-Shaw cell of width W. The thickness, b, of the cell is small compared to W (right). The front propagates at a constant velocity in the direction of the cell axis, Oz, from the product (of density ρ^-) to the reactant (of density ρ^+). Left: Oz is vertical and oriented downward, and the flat shaped reaction front propagates at the chemical velocity $\vec{V}_\chi$. Right: Oz is horizontal and the distorded reaction front propagates at the velocity $\vec{V}_f$.

$$\frac{\partial \vec{u}}{\partial t} + (\vec{u}\cdot\vec{\nabla})\vec{u} = -\frac{1}{\rho}\vec{\nabla}P + \vec{g} + \nu\Delta\vec{u}, \tag{7}$$

where $\nu = \eta/\rho$ is the kinematic viscosity. It has been observed that the coupling between the chemical reaction and the density driven flow results in a stationary distorted reaction front propagating along the cell axis at a constant velocity. Figure 1 is a sketch of a chemical reaction front in the plane (Oyz) of a Hele-Shaw cell of width W and thickness b. The front propagates from the product of density ρ^- to the reactant of density ρ^+, at the velocity $\vec{V}_f$, parallel to the cell axis, Oz.

A. Experiments

In the present work, we analyzed the stationary reaction fronts, observed at long times in tilted Hele-Shaw cells. In order to validate our model, we performed experiments with the IAA autocatalytic reaction in Hele-Shaw cells of width, $W=8$ mm, and thickness, $b=0.4$ mm, much smaller than the cell length. Polyvinyl alcohol (PVA) was used to detect the transient iodine of the reaction front [14] (see Fig. 4, left panel). The initial concentrations were fixed to: $[IO_3^-]_0 = 7.5$ mM, $[H_3AsO_3]_0 = 25$ mM and PVA at 6 kg m^{-3}.

The plane of the cell was held vertical, full of arsenous acid. The reaction was then initialized with a small amount of product at the top boundary of the cell, which was subsequently sealed. The chemical wave velocity was measured in this stable downward propagating configuration, and found in the range $V_\chi \in [10,14]$ μm s^{-1}. The cell was then tilted to the desired angle. The so-obtained chemical front did evolve toward a stationary-shaped front, traveling at a constant velocity, $\vec{V}_f$. The sketch of a chemical reaction front in Fig. 2 defines the front velocity, $\vec{V}_f$, parallel to the cell axis, Oz, the tilt angle, θ, of the cell axis with the gravity direction, and the unit vector, $\vec{n}$, normal to the front line at one front location, which gives the direction of the chemical reaction at that front location.

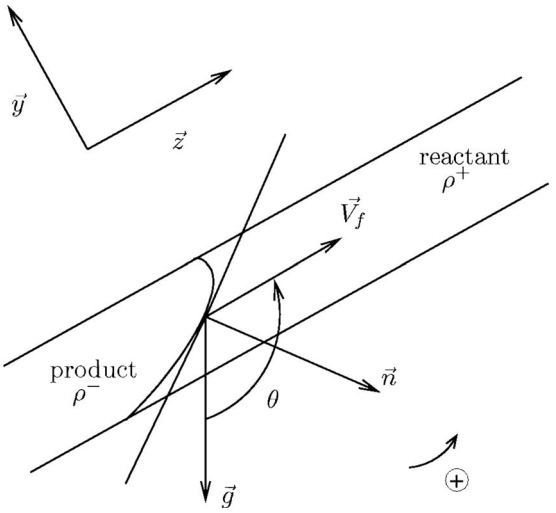

FIG. 2. Characterization of the stationary autocatalytic reaction front in the plane (Oyz) of a Hele-Shaw cell. The cell axis, Oz, is tilted by the angle θ with respect to the direction of the gravity vector, $\vec{g}$. The front propagates at the velocity $\vec{V}_f$, parallel to Oz. $\vec{n}$ denotes the local unit vector normal to the front.

B. Modelization and numerical method

The 2D simulations were carried out using a NSD (Navier-Stokes-Darcy)-ADR model [7,15], which was shown to efficiently account for the experimental dispersion curves measured on a buoyantly unstable IAA ascending front in a Hele-Shaw cell [5]. This model describes the time evolution of the gap-averaged concentration and fluid velocity, $C(y,z,t) = \frac{1}{b}\int_0^b c(x,y,z,t)dx$ and $\vec{U}(y,z,t) = \frac{1}{b}\int_0^b \vec{u}(x,y,z,t)dx$ through a set of two equations which, for inertialess flows, consists of:

(i) an advection-diffusion-reaction (ADR) equation,

$$\frac{\partial C}{\partial t} + \vec{U}\cdot\vec{\nabla}C = D(U)\Delta C + \alpha C^2(1-C) \tag{8}$$

(ii) and a Stokes-Darcy (SD) equation,

$$\vec{0} = -\frac{1}{\rho}\vec{\nabla}P - \frac{\nu}{K}\vec{U} + \frac{\Delta\rho}{\rho}C\vec{g} + \beta\nu\Delta\vec{U}, \tag{9}$$

where $K = \frac{b^2}{12}$ is the permeability of the Hele-Shaw cell and $\Delta\rho = \rho^+ - \rho^-$ is the density difference between the reactant and the product. In the present work we use the Boussinesq approximation [ρ is assumed to be constant in Eq. (9)]. The last term in the right hand side of Eq. (9) is the Brinkman correction to the Darcy equation. For the case of a Hele-Shaw cell, several values of the β prefactor can be found in the literature [16–18]. However, it was shown [18] that, in both cases of density stratification and no-slipping side wall conditions, β takes the value $\frac{12}{\pi^2}$. Accordingly we used this value in our simulations but we nevertheless investigated the impact of the coefficient on our results. Figure 3 displays the stationary front velocity as a function of the β parameter, for a cell aspect ratio, $W/b=10$. The variations of the front velocity do not exceed 5% for $\beta \in [0.5,1.4]$. Similarly, the

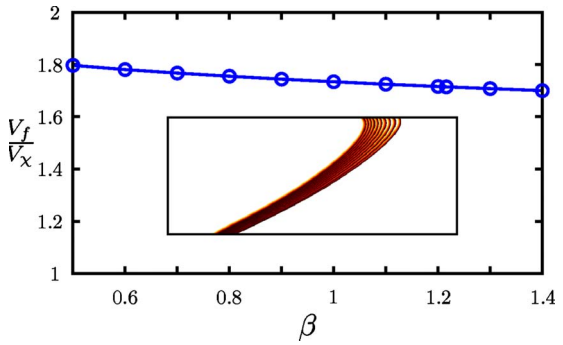

FIG. 3. (Color online) Effect of the Brinkman correction to the Darcy equation on the stationary-shaped chemical reaction front. The figure displays the normalized front velocities (dots) and the front profiles (inset) for a β prefactor [Eq. (9)] ranging between 0.5 and 1.4 (with a step 0.1) and a cell aspect ratio $\frac{W}{b}=10$. The other parameters are $\varepsilon=1.6$, $\Gamma_\chi=230$ [Eq. (12)]. The numerical simulations in this paper were performed with $\beta=\frac{12}{\pi^2}\simeq 1.22$.

front shape does not display any significant change with the value of β.

In Eq. (8), $D(U)$ is an effective diffusion coefficient which accounts for the dispersion enhancement due to the flow velocity profile in the gap. In the case of a passive tracer, an expression of $D(U)$ for the moderate velocity regime was obtained by Taylor [19],

$$D(U) = D_m + D_T \quad \text{with} \quad D_T = \frac{1}{210}\frac{(Ub)^2}{D_m}, \tag{10}$$

where D_m is the molecular diffusion coefficient. In the present case of an autocatalytic reaction, it has been shown [20,21] that the expression (10) also applies in the gap mixing regime ($b \ll l_\chi$).

A 2D lattice BGK method [22,23] was used to solve Eqs. (8) and (9) on grids of typical size 256×2048, with bounce-back boundary conditions for the fluid and the concentration. The accuracy of the numerical discretization was checked to give variations in the results less than 2% when the spatial resolution is varied by a factor two.

C. Dimensionless control parameters

In the literature, several dimensionless parameters have been proposed to delineate the different regimes in the presence of flow and chemical reaction propagation. The relative buoyancy strength may be estimated by two dimensionless parameters. One of them is the Rayleigh number, $\mathrm{Ra}=(b/L)^3$, where $L=(2\rho\nu D_m/\Delta\rho g)^{1/3}$ is the cutoff wavelength of the Rayleigh-Taylor instability in the case of an unbounded thin front [10,15,17]. The other one, $\varepsilon=V_g/V_\chi$, compares the chemical front velocity V_χ with the characteristic gravitational velocity

$$V_g = \frac{\Delta\rho g K}{\eta}, \tag{11}$$

which describes the balance between buoyancy and viscous forces in Eq. (9).

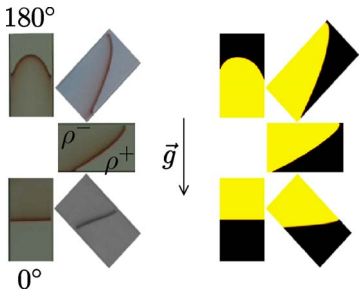

FIG. 4. (Color online) Qualitative comparison between experiments (left panel) and numerical simulations (right panel). The nondimensional quantities are $\varepsilon=\frac{V_g}{V_\chi}=1.6$, $\Gamma=\frac{W}{b}=20$ (where $b\times W=0.4\times 8$ mm^2) and $\Gamma_\chi=\frac{W}{l_\chi}=460$. The tilt angle θ varies from 0° to 180° (step 45°). $\theta=0°$ corresponds to a planar chemical reaction front, obtained in the buoyantly stable configuration, with the product lying over the reactant.

On another hand, the chemical reaction characteristic time $\tau_\chi=1/\alpha$ can be compared to different transport times. The Thiele modulus, $\Phi^2=\tau_D(b)/\tau_\chi$, compares τ_χ to the diffusive time across the gap of the cell, $\tau_D(b)=b^2/D_m$. The Damköhler number, $\mathrm{Da}=\tau_{adv}(l_\chi)/\tau_\chi$, compares τ_χ to a typical advective time along the front thickness, $\tau_{adv}(l_\chi)=l_\chi/V_g$. On can also define the Péclet number, $\mathrm{Pe}_\chi=\tau_D(b)/\tau_{adv}(l_\chi)$, which has been shown to be the relevant parameter to delineate the Taylor's regime [21].

In our case of interest, because of the large aspect ratio of the cell, W has also to be considered. It may be compared either to b or to l_χ through $\Gamma=W/b$ and $\Gamma_\chi=W/l_\chi$, respectively.

Among the different dimensionless parameters, we can show that only three are needed to describe the system. In the following, we will use:

$$\varepsilon = \frac{V_g}{V_\chi}, \quad \Gamma = \frac{W}{b}, \quad \Gamma_\chi = \frac{W}{l_\chi} \tag{12}$$

and discuss this choice later on. We note that the previously defined numbers may be rewritten as: $\mathrm{Ra}=6\varepsilon\Gamma_\chi/\Gamma$, $\Phi^2=2(\Gamma_\chi/\Gamma)^2$, $\mathrm{Da}=2/\varepsilon$, and $\mathrm{Pe}_\chi=\varepsilon(\Gamma_\chi/\Gamma)^2$.

D. Comparison between experiments and numerical simulations

Figure 4 shows the stationary front shapes obtained, in experiments (left panel of Fig. 4) and with numerical simulations (right panel of Fig. 4), when the tilt angle, θ, is varied. It can be noticed that the front shape is flat for $\theta=0°$, which corresponds to the buoyancy stable configuration of the product of density ρ^- lying above the reactant of density ρ^+. When θ increases, buoyancy effects come into play, and the chemical reaction front adapts its shape and its velocity to the new external condition. We obtain a curved front, which may be characterized by its velocity, V_f, and by its extension, E. Here, we defined the front extension as the distance along the cell axis, $E=z_1-z_2$, between the locations of the transverse averaged concentrations $\langle C\rangle_y(z_1)=0.01$ and $\langle C\rangle_y(z_2)=0.99$.

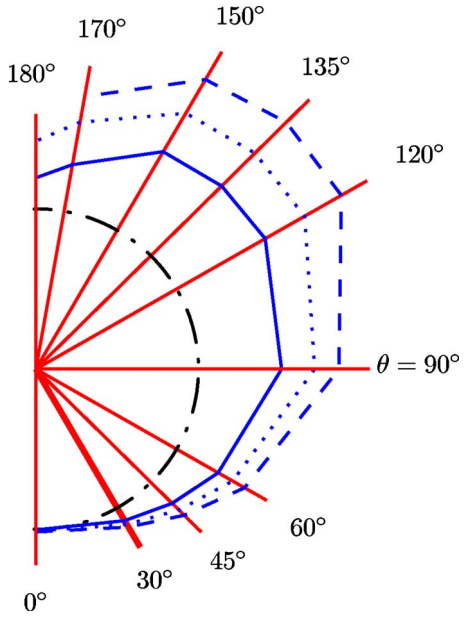

FIG. 5. (Color online) Numerical simulations. Chemical front velocity, V_f, normalized by the chemical velocity, V_χ, as a function of the tilt angle, θ, in a polar coordinates system. The numerical simulations were performed for angles θ varying between 0° and 180° (straight lines). The different curves were obtained at $\varepsilon=1.6$ and correspond to different cell widths, W, whereas the thickness of the cell, b, remains constant. $\Gamma=5$ (–), 10 (···) and 20 (– –), and $\Gamma_\chi=23\Gamma$. The dash-dotted line corresponds to $\frac{V_f}{V_\chi}=1$.

Figure 5 displays in a polar coordinates system, the reaction front velocity, V_f, normalized by the chemical velocity, V_χ, obtained with numerical simulations, for tilt angles θ between 0° and 180°.

The simulations were performed for three different cell widths W and a constant cell gap b, corresponding to $\Gamma=W/b=5$, 10, and 20. One notices that, for $\theta=0°$, V_f is equal to V_χ for all Γ values. V_f increases with θ, up to a maximum value, of the order of a few units of V_χ, for an angle θ lying between 120° and 150°. The value of the maximum front velocity increases with Γ, as well as the front velocity at any fixed angle θ. This representation allows a comparison with the experiments in a tube by Nagypal *et al.* [9] who observed the same trends, with a maximum front velocity for a tilt angle between 90° and 180°.

A quantitative comparison between the front velocities measured in our experiments in a Hele-Shaw cell and in the numerical simulations is displayed in Fig. 6. The front velocities are plotted versus the tilt angle, for different sets of experiments. The agreement between the experiments and the numerical simulations is rather good. Note that although the same protocol was used, the experimental data exhibit some dispersivity, which is most likely due to the uncertainty on V_χ and to the reaction initiation procedure. As a consequence, numerical simulations may be more suitable to carry out a parametric study.

III. NUMERICAL SIMULATIONS

In the following, we will present a numerical investigation of the effect of the three dimensionless parameters ε, Γ, and Γ_χ. Figure 7 displays the front location together with the vector field of the fluid velocity obtained for different tilt angles. A buoyantly driven convection roll is observed for any tilt angle, $\theta\in]0°,180°[$. The flow is supportive (same direction as the chemical front propagation) at the upper boundary (at $y=W/2$, see Fig. 1), and is adverse at the lower boundary ($y=-W/2$). The evolution of the roll intensity with the tilt angle is similar to that of the front velocity. In particular, it is maximum for $\theta\simeq135°$ and we note that the increase of the roll intensity is accompanied by an increasing leaning of the front over the lower boundary of the cell. Also the location of the induced roll is linked with that of the front: The center of the roll is found on the front (close to the middle of the cell). Moreover, we tracked the maximum value, U_{max}, of the fluid velocity field: It always corresponds to a velocity vector aligned with Oz, at the very location where the front is normal to Oz. Note that in vertical cells, two particular behaviors are observed. For $\theta=0°$, the fluid is at rest, and for $\theta=180°$, two counter rotating rolls are gener-

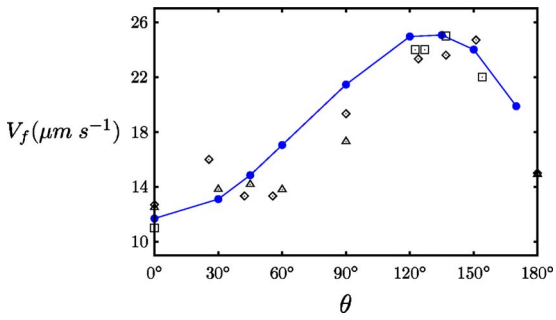

FIG. 6. (Color online) Front velocity measured in the experiments and in the simulations, versus the tilt angle, θ. The symbols correspond to different runs of experiments, and the dots connected by a line to the numerical simulations. $\varepsilon=1.6$, $\Gamma=20$, and $\Gamma_\chi=460$ were kept constant.

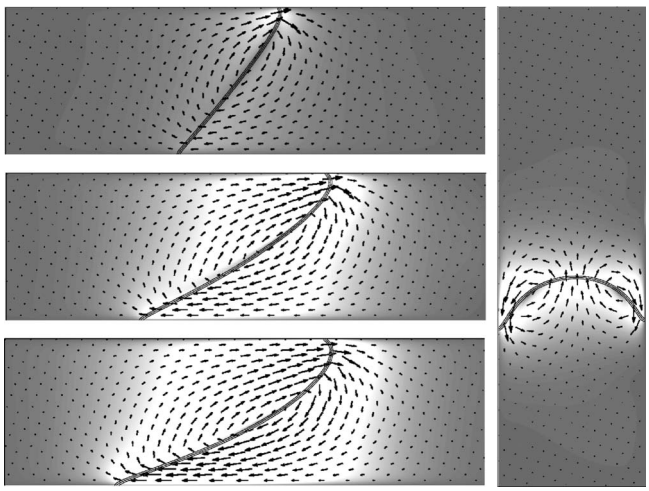

FIG. 7. Effect of the buoyancy contrast on the velocity field. Left panel, from top to bottom: Tilt angle, $\theta=45°$, 90°, and 135°. Right: $\theta=180°$. The shade off gray represents the intensity of velocity. The isocontours $C=0.1$, $C=0.5$ and $C=0.9$ (solid lines), are very close to one another and reflect the narrowness of the front. $\varepsilon=3.6$, $\Gamma=10$, $\Gamma_\chi=230$.

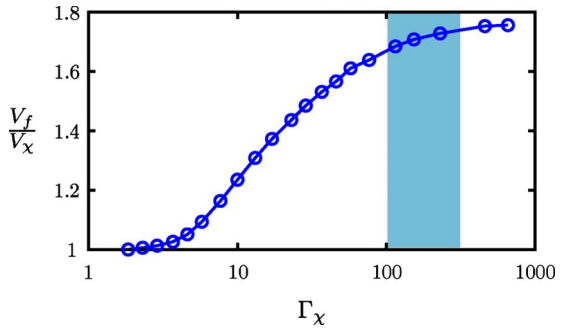

FIG. 8. (Color online) Normalized chemical reaction front velocity, $\frac{V_f}{V_\chi}$, versus the nondimensional geometrical parameter $\Gamma_\chi = \frac{W}{l_\chi}$, at $\theta=90°$, $\varepsilon=1.6$, $\Gamma=10$. The numerical simulation results (dots) are linked by a line. The curve shows the transition between the mixing regime at small Γ_χ and the eikonal regime at large Γ_χ. The shaded region displays the range explored by the experiments and the numerical simulations of this paper.

ated (Fig. 7, right), similar to the observations by [24,25]. In the latter case, the flow is supportive in the middle of the cell plane and adverse near the walls.

A. Influence of the front thickness

The propagation of an autocatalytic reaction front is known to have two asymptotic regimes, namely, the mixing one at large front thickness l_χ and the eikonal one at $l_\chi \simeq 0$. As discussed above, our model addresses the mixing regime ($l_\chi \simeq b$) in the cell gap. However, in the plane of the cell, both regimes may still be found depending on the value of $\Gamma_\chi = W/l_\chi$.

Figure 8 shows the evolution of the normalized front velocity with Γ_χ, at $\theta=90°$, $\varepsilon=1.6$, and $\Gamma=10$. As expected, in the mixing regime, $\Gamma_\chi \to 0$, buoyancy is inhibited, and thus, in the absence of induced flow, the chemical velocity V_χ is recovered. Note that the mixing regime applies for W values up to several l_χ. On the opposite, V_f approaches a maximum value for $\Gamma_\chi \simeq 1000$ (eikonal regime). We will use in the following, values of Γ_χ of the order of a few hundreds (as in the experiments). For such values of Γ_χ, the behavior is close to the eikonal regime, and should not be very sensitive to the specific value of Γ_χ. This assertion is confirmed in Fig. 9, which displays the front velocity as a function of the tilt angle θ for two different Γ_χ. This behavior is in contrast with the one obtained by [10] in Stokes flows, where an increase of the front velocity was observed for a normalized distance between the no-slip boundaries ranging between 5 and 20. We note however that this range corresponds to the intermediate regime (see Fig. 8).

In the eikonal regime, which applies when the front thickness is small compared to the front deformation scale, the gap-averaged ADR Eq. (8) can be replaced by the so-called eikonal equation:

$$\vec{V}_f \cdot \vec{n} = \vec{U} \cdot \vec{n} + V_\chi + D(U)\kappa, \tag{13}$$

where D is the macroscopic diffusion coefficient, κ is the front curvature and $\vec{V}_f \cdot \vec{n}$ is the local interface velocity, which

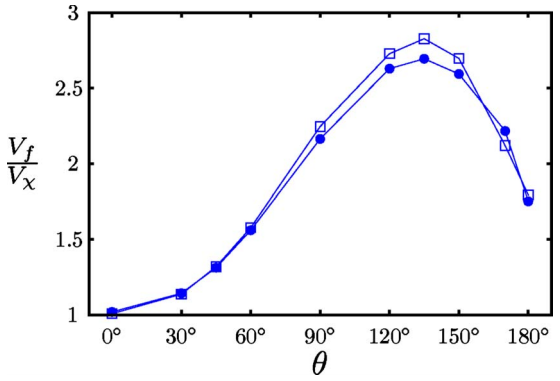

FIG. 9. (Color online) Normalized front velocity, $\frac{V_f}{V_\chi}$, versus θ, for two values of Γ_χ. $\Gamma_\chi=120$ (●) and 230 (□). $\varepsilon=3$, $\Gamma=10$.

measures the propagation velocity along the direction, $\vec{n}$, normal to the interface. Moreover, the eikonal regime conditions, $1/\kappa \gg l_\chi$, imply that $(D\kappa)$ must be a second order correction, when compared to V_χ, so that Eq. (13) may be approximated by the simplified eikonal equation,

$$\vec{V}_f \cdot \vec{n} - V_\chi = \vec{U} \cdot \vec{n}, \tag{14}$$

where the front curvature has been neglected. Figure 10 displays a typical profile of the local interface velocity enhancement, $\vec{V}_f \cdot \vec{n} - V_\chi$, together with the normal component of the fluid velocity, $\vec{U} \cdot \vec{n}$. The rather good agreement between the two curves indicates that the simplified Eq. (14) does apply. We note that the maxima of the two curves differ in amplitude by a small amount, of about 8%, which may be attributed to the neglected front curvature, but they are found at the same location y. At this location, the interface is perpendicular to Oz, since the maximum, $V_f - V_\chi$, of the left hand side of Eq. (14) is reached for $\vec{n} \cdot \vec{z} = 1$. At the same time, the maximum of the right hand side of Eq. (14) is equal to the fluid velocity maximum value, U_{max}, as the latter was found to correspond to a fluid velocity vector located on the front and aligned with $\vec{n} = \vec{z}$. Thus, the front velocity enhancement $V_f - V_\chi$ can be estimated from the velocity field alone, as $V_f - V_\chi \simeq U_{max}$. Moreover, using Eq. (14), one can infer the position and the shape of the front from the velocity field,

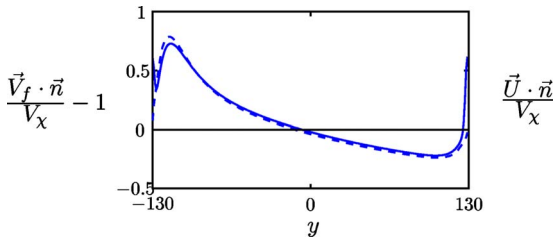

FIG. 10. (Color online) Typical velocity profiles in the plane of the Hele-Shaw cell. Normalized local interface velocity enhancement, $\frac{\vec{V}_f \vec{n}}{V_\chi} - 1$, with respect to the chemical velocity, V_χ (solid line), and normalized fluid velocity normal component, $\frac{\vec{U} \cdot \vec{n}}{V_\chi}$ (dashed line), versus the coordinate y. The two quantities are very close to each other, as expected in the eikonal regime. $\theta=90°$, $\varepsilon=1.6$, $\Gamma=10$, $\Gamma_\chi=230$.

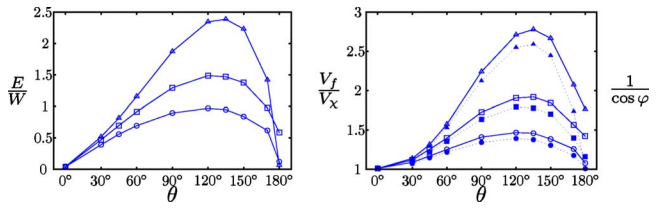

FIG. 11. (Color online) Left: extension, E, of the chemical reaction front, normalized by the cell width, W, versus the tilt angle, θ, for three values of ε. Right: normalized front velocity, $\frac{V_f}{V_\chi}$ (open symbols), versus θ, compared with the simplified eikonal estimation, $\frac{1}{\cos\varphi}=\sqrt{1+(\frac{E}{W})^2}$, given by Eq. (15) (full symbols), for three values of ε. $\varepsilon=0.8$ (○), 1.6 (□) and 3.2 (△), $\Gamma=10$, $\Gamma_\chi=230$.

and they are such that the front propagates along Oz at the highest velocity enabled by Eq. (14) for the given fluid velocity field. This property which was already established for the stationary front propagation in a fixed unidirectional periodic flow field $\vec{U}=U(y)\vec{z}$ [20,26] must be then a robust property of the stationary eikonal regime. But we recall that in the present case, the flow is induced by the reaction itself. Then, although the flow intensity, U_{max}, and thus V_f-V_χ, is known to scale with V_g, numerical simulations are needed to measure it. We also note that the simplified eikonal equation provides also an alternative estimation of V_f from the angle, $\varphi=(\vec{n},\vec{z})$, at the front location where $\vec{U}.\vec{n}=0$: $V_f\cos\varphi=V_\chi$. A rough estimation of φ, assuming a straight front, may be obtained using the extension length of the front, E, and the geometrical relation $\tan\varphi\simeq E/W$. This leads to:

$$V_f\simeq\frac{V_\chi}{\cos\varphi}=V_\chi\sqrt{1+\left(\frac{E}{W}\right)^2}. \tag{15}$$

Figure 11 represents the normalized extension, E/W, and the normalized front velocity, V_f/V_χ, obtained for three different values of the parameter ε, as functions of the tilt angle. Both quantities display a similar behavior. Moreover, Eq. (15) gives a rather good (also slightly underestimated) prediction of the front velocity. This demonstrates that the front velocity and the extension are linked in our eikonal regime. Accordingly, we will focus only on the V_f measurement in the following.

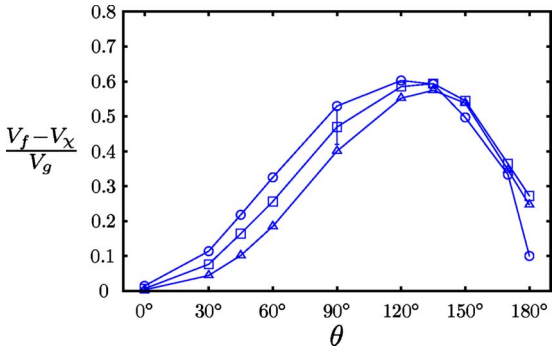

FIG. 12. (Color online) Front velocity enhancement, V_f-V_χ, normalized by the gravitational velocity, V_g, versus θ. $\varepsilon=0.8$ (○), 1.6 (□) and 3.2 (△), $\Gamma=10$, $\Gamma_\chi=230$.

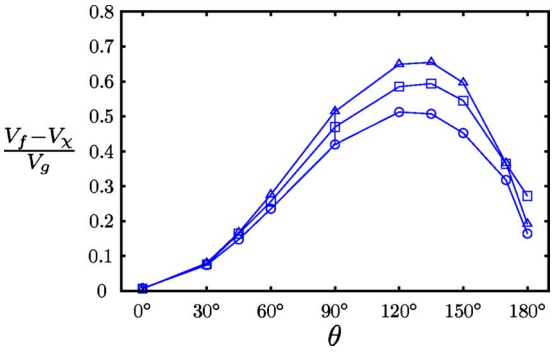

FIG. 13. (Color online) Front velocity enhancement, V_f-V_χ, normalized by the gravitational velocity, V_g, versus θ, for three values of Γ. $\Gamma=7$ (○), 10 (□) and 14 (△), $\varepsilon=1.6$, $\Gamma_\chi=230$.

B. Influence of buoyancy

As expected, one can see on Fig. 11 that both E and V_f increase strongly with the buoyancy parameter $\varepsilon=V_g/V_\chi$. Figure 11 suggests also that the front velocity enhancement V_f-V_χ may vary linearly with ε. Indeed, an alternative normalization of V_f-V_χ by V_g leads to a rather good collapse of the curves, as shown in Fig. 12. Note that this behavior is consistent with the scaling $E/W\propto\varepsilon$ for the fully developed unstable front in a homogeneous porous medium [8]. On the contrary, it is in contrast with the results of [10], devoted to the study of a Stokes flow in the intermediate regime (between mixing and eikonal). In that work, the front velocity was reported to vary with $\sqrt{\mathrm{Ra}}$, leading to $V_f\propto\sqrt{\varepsilon}$, whereas our results show that $V_f-V_\chi\propto\varepsilon$.

C. Influence of the cell thickness

We now investigate the influence of the parameter $\Gamma=W/b$. The normalized velocity enhancement $(V_f-V_\chi)/V_g$ as a function of θ was computed for three different values of Γ, at $\varepsilon=1.6$ and $\Gamma_\chi=230$ (see Fig. 13). The three curves are close to one another. However, doubling the value of Γ leads to a relative difference of 25% in the maximal values of the curves. This significant discrepancy may be related to the Brinkman term in Eq. (9). An insight into this effect is given by Fig. 14, which displays, for different Γ, the fluid velocity profiles along the front, versus the distance from the lower wall, normalized by W and b (Fig. 14, left and right, respec-

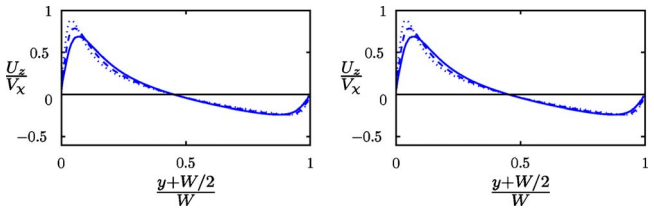

FIG. 14. (Color online) Fluid velocity profiles along the front as functions of the distance from the lower wall, $y+W/2$, normalized by W (left) and b (right), for different values of Γ. The figures show that the velocity profile scales with W in the central part of the cell (left) and with b close to the boundary (right). $\Gamma=7$ (–), 10 (– –) and 14 (···), $\varepsilon=1.6$, $\Gamma_\chi=230$.

tively). Figure 14, left, shows that the spatial variation of the fluid velocity scales with W on mostly all the domain except in the vicinity of the walls. In these regions, the no-slip condition at the wall affects the flow field over a distance of the order of b, as shown in Fig. 14, right. This scaling is expected from the Brinkman term in Eq. (8) and may slightly vary with the β parameter (see Fig. 3). Accordingly, $b/W = 1/\Gamma$ should give an estimate of the damping of the flow by the no-slip condition. This explains the behavior observed in Fig. 13, where the front velocity decreases with $1/\Gamma$.

IV. COMPARISON WITH OTHER SYSTEMS

Our simulations have used the kinetics of an IAA reaction, but our results may however apply to other similar autocatalytic reactions. Recent experiments were performed with the Chlorite-Tetrathionate (CT) autocatalytic reaction [11] in Hele-Shaw cells. They focused on the effect on the chemical front extension (called mixing length, L_m, in that paper), of the aspect ratio (from $\Gamma=10$ to $\Gamma=40$) and of the initial chemical composition (from $[S_4O_6^{2-}]=3.75$ to 6.25 mM). The commonly reported values of V_χ and D_m as functions of the chemical composition for the CT (see [27]) lead to an estimation of $\Gamma_\chi > 100$. Accordingly, the eikonal regime addressed in our simulations should apply. We have shown that, at a given Γ, the chemical front extension is linear with ε and does not depend on Γ_χ. For the CT reaction [11,27], $V_\chi \propto [S_4O_6^{2-}]^{3/2}$ and $\Delta\rho \propto [S_4O_6^{2-}]$, leading to $\varepsilon \propto [S_4O_6^{2-}]^{-1/2}$. As a result, ε, and hence E, varies only within $\pm 15\%$ in the covered range of concentrations. This is in line with the independence of the mixing length, L_m, with the chemical reaction observed in [11]. Moreover, the measured values of the front extension are in the range of our simulations. We measured in Fig. 11, $E/W \simeq 1.9$ for $\theta=90°$, $\varepsilon=3.2$, and $\Gamma=10$. This aspect ratio corresponds in the CT experiment [11] to $W=L_y=1$ cm, for which a measured value of E is $E \simeq 4L_m \simeq 2.2$ cm, in reasonable agreement with our simulations. In our simulations the variations of Γ from 7 to 14 leads to a variation of E/W of 1.15 ± 0.05 consistent with the power law used in [11]: $2^{0.19} \simeq 1.14$.

V. DISCUSSION AND CONCLUSION

We have analyzed the solutal buoyancy effect on the shape and the velocity of autocatalytic reaction fronts, propagating in thin tilted rectangular channels. We used 2D lattice BGK numerical simulations of gap-averaged equations for the flow and the concentration, namely a Stokes-Darcy equation coupled with an advection-diffusion-reaction equation. We did observe stationary-shaped fronts, spanning the width of the cell plane and propagating along the cell axis. We have shown that the local front shape is linked to the traveling velocity with an eikonal equation involving the local fluid velocity. Moreover, this regime leads to a simple relation between the velocity and the extension of the front:

$$V_f \simeq V_\chi \sqrt{1 + \left(\frac{E}{W}\right)^2}. \tag{16}$$

We have performed a parametric study using $\varepsilon = V_g/V_\chi$, $\Gamma = W/b$ and $\Gamma_\chi = W/l_\chi$. The normalized front velocity enhancement was found to be proportional to ε,

$$V_f/V_\chi - 1 = \varepsilon G(\Gamma, \Gamma_\chi), \tag{17}$$

where the function G, represented in Figs. 12 and 13, varies weakly with Γ (within 20% when Γ is doubled) and remains nearly constant at large values of $\Gamma_\chi (\Gamma_\chi \gg 1)$. The so-obtained behavior justifies the relevance of the three nondimensional parameters used and suggests a scaling of $V_f - V_\chi$ with V_g. Our results account rather well for experiments we performed using an Iodate Arsenous Acid reaction propagating in tilted Hele-Shaw cells. Moreover, our 2D modelization enables also some comparison with results found for another chemical reaction (chlorite tetrathionate) in similar conditions [11].

ACKNOWLEDGMENTS

This work was partly supported by CNES (Grant No. 793/CNES/00/8368), ESA (Grant No. AO-99-083), Réseaux de Thématiques de Recherches Avancées 'Triangle de la Physique' and the Initial Training Network (ITN) "Multiflow." I. BouMalham was supported by a grant from the CNRS and N. Jarrige by a grant from the French Ministry of Research (MESR). All these sources of support are gratefully acknowledged.

[1] R. Fisher, Ann. Eugen. **7**, 355 (1937).
[2] A. Kolmogorov, I. Petrovsy, and N. Piskounov, Applicable Mathematics of Non-Physical Phenomena (1937).
[3] A. Hanna, A. Saul, and K. Showalter, J. Am. Chem. Soc. **104**, 3838 (1982).
[4] S. K. Scott, *Oscillations, Waves, and Chaos in Chemical Kinetics*, Physical (Oxford University Press, New York, 2004), Vol. 18.
[5] M. Böckmann and S. C. Müller, Phys. Rev. Lett. **85**, 2506 (2000).
[6] J. A. Pojman and I. R. Epstein, J. Phys. Chem. **94**, 4966 (1990).
[7] J. Martin, N. Rakotomalala, D. Salin, and M. Böckmann, Phys. Rev. E **65**, 051605 (2002).
[8] A. De Wit, Phys. Fluids **16**, 163 (2004).
[9] I. Nagypal, G. Bazsa, and I. R. Epstein, J. Am. Chem. Soc. **108**, 3635 (1986).
[10] L. Rongy, N. Goyal, E. Meiburg, and A. De Wit, J. Chem. Phys. **127**, 114710 (2007).
[11] G. Schuszter, T. Toth, D. Horvath, and A. Toth, Phys. Rev. E **79**, 016216 (2009).
[12] Y. Qian, D. D'Humières, and P. Lallemand, EPL **17**, 479 (1992).
[13] J. A. Pojman, I. R. Epstein, T. J. McManus, and K. Showalter,

J. Phys. Chem. **95**, 1299 (1991).
[14] T. Yoshinaga, M. Tsuschida, Y. Toyose, H. Hiratsuka, and M. Yamaye, Anal. Sci. **20**, 549 (2004).
[15] J. Huang and B. F. Edwards, Phys. Rev. E **54**, 2620 (1996).
[16] C. Ruyer-Quil, C. R. Acad. Sci., Ser. IIb Mec. **329**, 337 (2001).
[17] J. Martin, N. Rakotomalala, and D. Salin, Phys. Fluids **14**, 902 (2002).
[18] J. Zeng, Y. C. Yortsos, and D. Salin, Phys. Fluids **15**, 3829 (2003).
[19] G. I. Taylor, Proc. R. Soc. London, Ser. A **219**, 186 (1953).
[20] M. Leconte, J. Martin, N. Rakotomalala, and D. Salin, J. Chem. Phys. **120**, 7314 (2004).
[21] M. Leconte, N. Jarrige, J. Martin, N. Rakotomalala, D. Salin, and L. Talon, Phys. Fluids **20**, 057102 (2008).
[22] E. G. Flekkøy, Phys. Rev. E **47**, 4247 (1993).
[23] L. Talon, J. Martin, N. Rakotomalala, D. Salin, and Y. Yortsos, Water Resour. Res. **39**, 1135 (2003).
[24] J. Masere, D. A. Vasquez, B. F. Edwards, J. W. Wilder, and K. Showalter, J. Phys. Chem. **98**, 6505 (1994).
[25] D. A. Vasquez, J. M. Littley, J. W. Wilder, and B. F. Edwards, Phys. Rev. E **50**, 280 (1994).
[26] B. Audoly, H. Berestycki, and Y. Pomeau C. R. Acad. Sci. Paris, Ser. II **328**, 255 (2000).
[27] A. Toth, D. Horvath, and A. Siska, J. Chem. Soc. **93**, 73 (1997).